（ ※本報告書は英語で記述してください。ただし、産業利用課題として採択されている方は日本語で記述していただいても結構です。 ）

CROSS TOKAI **Experimental Report** J-PARC	承認日 Date of Approval 承認者 Approver 提出日 Date of Report
課題番号 Project No. 2014E0003 実験課題名 Title of experiment In-situ Neutron Analysis of Advanced Structural Materials in Elements Strategy Initiative for Structural Materials (ESISM) 実験責任者名 Name of principal investigator Nobuhiro Tsuji 所属 Affiliation Kyoto University	装置責任者 Name of Instrument scientist BL14: Kenji Nakajima BL:19: Kazuya Aizawa 装置名 Name of Instrument/(BL No.) BL14, BL19 実施日 Date of Experiment BL14: 6/23-6/26, 2014 BL19: (1)11/13-11/18, 2014 (2) 3/28-3/30, 2015

試料、実験方法、利用の結果得られた主なデータ、考察、結論等を、記述して下さい。(適宜、図表添付のこと)
Please report your samples, experimental method and results, discussion and conclusions. Please add figures and tables for better explanation.

1. 試料 Name of sample(s) and chemical formula, or compositions including physical form.

BL19: (1) 11/13-11/18, 2014

Fe-2Mn-0.1C (wt. %), Fe-2Mn-0.4C (wt. %), Fe-6Ni-0.1C (wt. %).

BL19: (2) 3/28-3/30, 2015

Fe-24Ni-6Al-0.4C (wt. %), Fe-1.7Mn-0.08C (wt. %), Cu-40Zn (wt. %), IF steel.

BL14: 6/23-6/26, 2014

Single crystal of the δ_{1p} phase ($Fe_{13}Zn_{126}$) with approximate dimension of φ8×L15 mm.

2. 実験方法及び結果（実験がうまくいかなかった場合、その理由を記述してください。）
Experimental method and results. If you failed to conduct experiment as planned, please describe reasons.

BL19: (1) 11/13-11/18, 2014

Dynamic ferrite transformation behavior was investigated by in-situ neutron diffraction analysis during compression at elevated temperature using a newly developed thermomechanical processing simulator installed at BL 19.

The thermomechanical processing simulator and a schematic illustration for an alignment of a specimen with respect to incident and diffracted neutron beams are shown in Fig.1. The specimen was austenitized at 850 °C for 300 s (Fe-2Mn-0.1C) or 800 °C for 180 s (Fe-2Mn-0.4C, Fe-6Ni-0.1C), and cooled to the deformation temperature ranging from 650 – 820 °C. Then, uniaxial compressive

2. 実験方法及び結果（つづき） Experimental method and results (continued)

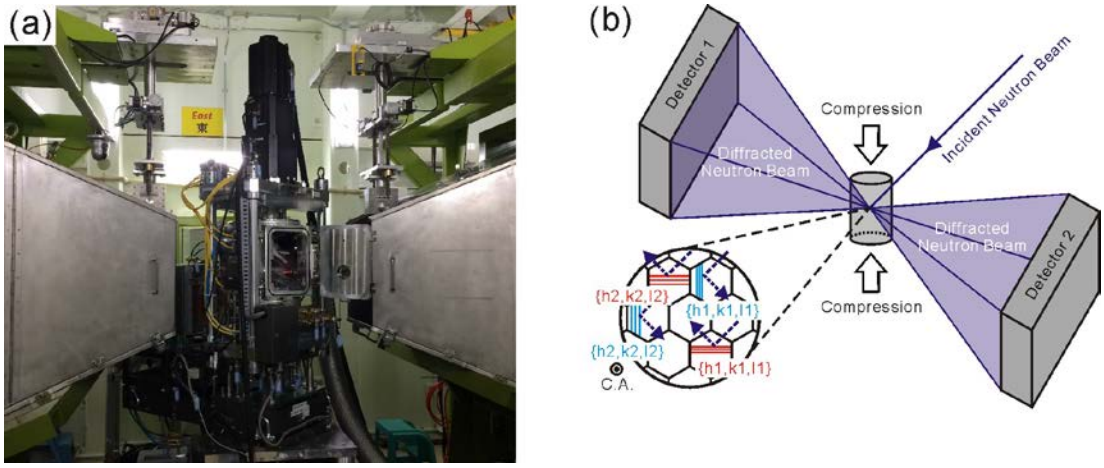

Figure 1 (a) The newly developed thermomechanical processing simulator installed at BL19, (b) schematic illustration showing an alignment of a compression specimen with respect to incident and diffracted neutron beam.

deformation by at most 60 % was applied at the temperature. The strain rate ($\dot{\varepsilon}$) was ranging from 1 × 10^{-1} s^{-1} to 2 × 10^{-4} s^{-1}. The specimen was placed between two anvils (Si_3N_4) in the chamber, and heated by induction heating system. The chamber moves upward by the half of deformation amount so that neutron beam is always irradiated at the center of the specimen during compression experiment. The result of experiment using the Fe-2Mn-0.1C alloy are shown below.

Fig. 2 shows a neutron diffraction profile of the Fe-2Mn-0.1C during compression experiment at 700 °C ($\dot{\varepsilon}$ = 1.0 × 10^{-3} s^{-1}). The horizontal and vertical axes correspond to time-of-flight (TOF) and time, respectively. The intensity of neutron diffraction is represented by change in color. It is clear that ferrite peaks started to appear during compression. As a result, we demonstrated from Fig.2 that dynamic ferrite transformation surely occurred during deformation, not after deformation.

Fig. 3 shows fractions of static ferrite transformation (without compression) and dynamic ferrite transformation (with compression) in the Fe-2Mn-0.1C alloy at 650 °C, 680 °C, and 700 °C as a function of time after reaching the temperature. Data for static ferrite transformation and dynamic ferrite transformation are shown in squares and circles, respectively, in Fig. 3. We found that the fraction of dynamically transformed ferrite was much higher than that of statically transformed ferrite. This indicates that the compressive deformation accelerated ferrite transformation significantly.

Changes in lattice constants of austenite and ferrite during static and dynamic ferrite transformations were

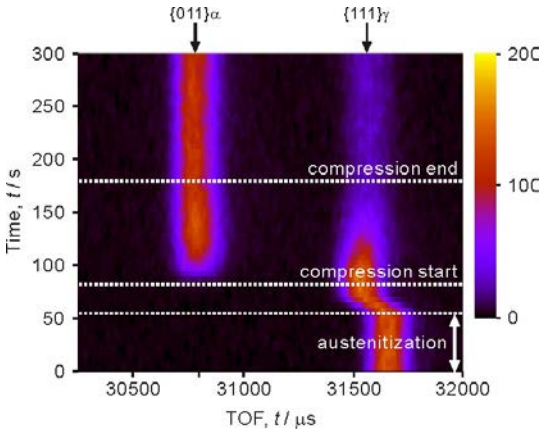

Figure 2 Color map showing the intensity of neutron diffraction peaks (enlarged region around {111}γ and {011}α) in compression of the Fe-2Mn-0.1C alloy as functions of TOF and time.

analyzed by Rietveld method using the software of Z-Rietveld. The results are shown in Fig.4. We found from Fig. 4(a) that the lattice constant of austenite gradually increased during static ferrite transformation (squares). This is because C content in austenite increased during transformation. In dynamic ferrite transformation (circles), on the other hand, the lattice constant of austenite increased significantly and kept constant after completion of compression. Because the diffraction planes in the specimen were parallel to the compression direction as shown in Fig. 2(b), compressive deformation induced elastic strain which expanded the spacing of diffraction planes. Therefore the increase in lattice constant of austenite during dynamic ferrite transformation was attributed to the elastic strain by compressive deformation and increase of C content diffused from formed ferrite. As shown in Fig. 4(b), the lattice constant of statically transformed ferrite (squares) did not change during transformation. In contrast, the lattice constant of dynamically transformed ferrite (circles) decreased during transformation, in particular at the later stage of transformation. It should be noted that the decrease in lattice constant of dynamically transformed ferrite was opposite tendency from the elastic strain by compressive deformation. We suppose that the initially transformed ferrite in dynamic transformation contained supersaturated Mn and C. The observed decrease of lattice constant of dynamically transformed ferrite would be attributed to partitioning of Mn and C to austenite during transformation.

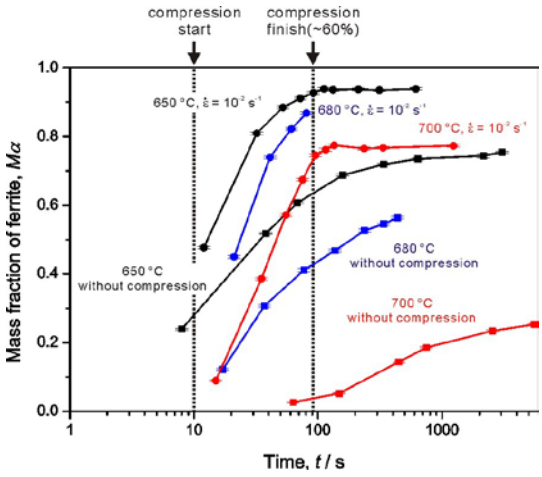

Figure 3 Changes in mass fractions of statically transformed ferrite (squares) and dynamically transformed ferrite (circles) as a function of time after reaching the temperature at 650 °C, 680 °C, and 700 °C.

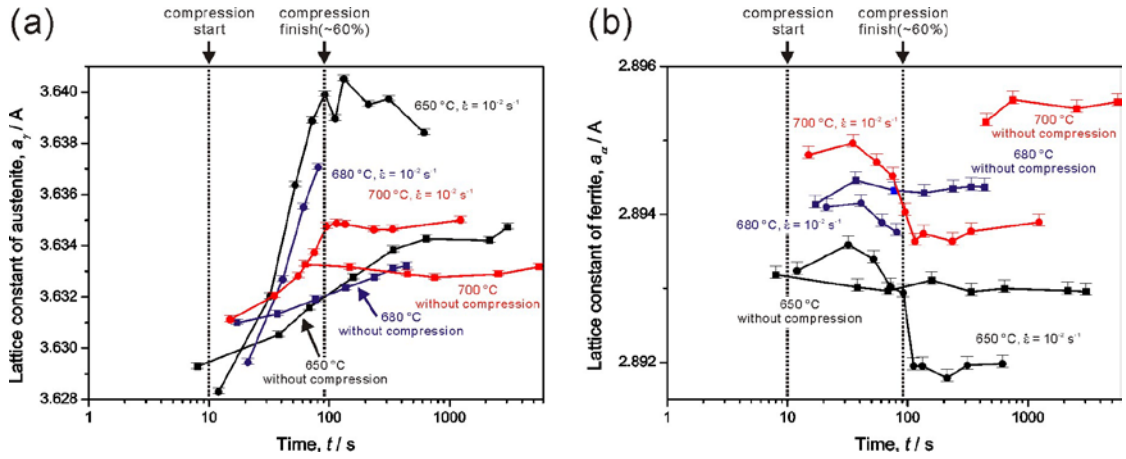

Figure 4 Changes in lattice constants of (a) austenite and (b) ferrite during static ferrite transformation (squares) and dynamic ferrite transformation (circles).

BL19: (2) 3/28-3/30, 2015

Two kinds of in-situ neutron diffraction experiments were conducted;

(i) Phase transformation behavior during tensile deformation in an Fe-24Ni-6Al-0.4C (wt. %) alloy.

(ii) Deformation behavior of a dual phase steel (Fe-1.7Mn-0.08C (wt. %)), a dual phase Cu-Zn alloy (Cu-40Zn (wt. %)), and an ultrafine-grained IF steel.

(i)

The cold-rolled Fe-24Ni-6Al-0.4C alloy exhibits extremely high strength but keeps reasonable elongation even in the as-rolled state. In order to clarify the origin of the superior mechanical properties, we investigated the phase transformation behavior of as-homogenized and cold-rolled Fe-24Ni-6Al-0.4C alloys by neutron diffraction analysis during tensile deformation.

Fig. 5 is a schematic illustration showing an arrangement of a tensile test specimen with respect to incident and diffracted neutron beams. Neutron diffraction profiles for tensile direction and normal direction of the sheet-type specimen was measured simultaneously.

Fig. 6 summarizes changes in integral intensities of each peak for tensile direction with increasing the strain analyzed from neutron diffraction profiles in as-homogenized specimen (a) and cold-rolled specimen (b). The as-homogenized specimen before tensile deformation consisted of austenite (FCC) and intermetallic particles (BCC base structure). On the other hand, the cold-rolled specimen was composed of austenite (FCC), intermetallic particles (BCC base structure), and martensite (BCC). As shown in Fig. 6, {011} peak of bcc phase increased with increasing the strain in both the as-homogenized specimen and the cold-rolled specimen. This indicates that deformation-induced martensitic transformation occurred during tensile deformation. Accordingly, the high strength and large ductility of the Fe-24Ni-6Al-0.4C alloy would be due to the transformation induced plasticity happened by deformation-induced martensitic transformation.

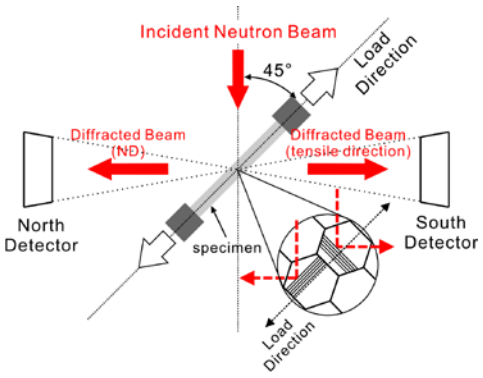

Figure 5 Schematic illustration showing an alignment of a tensile test specimen with respect to incident and diffracted neutron beam.

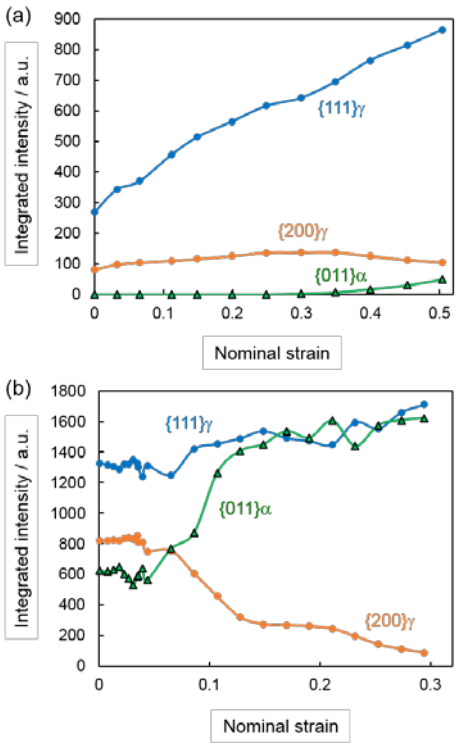

Figure 6 Changes in integral intensities of neutron diffraction peaks for the tensile direction with increasing the strain. (a) the as-homogenized specimen, (b) the cold-rolled specimen.

(ii)

Deformation behaviors of the dual phase steel, the dual phase Cu-Zn alloy, and the ultrafine-grained IF steel were investigated by in-situ neutron diffraction analysis during tensile deformation. The procedure was the same as described in (i) (Fig.5). One example of neutron diffraction profiles of the dual phase steel during tensile deformation are shown in Fig.6. Based on these neutron diffraction profiles, we are now analyzing stress and strain partitioning behaviors during tensile deformation in the dual phase steel and dual phase Cu-Zn alloy. We are also analyzing change in dislocation density of the ultrafine-grained IF steel during tensile deformation.

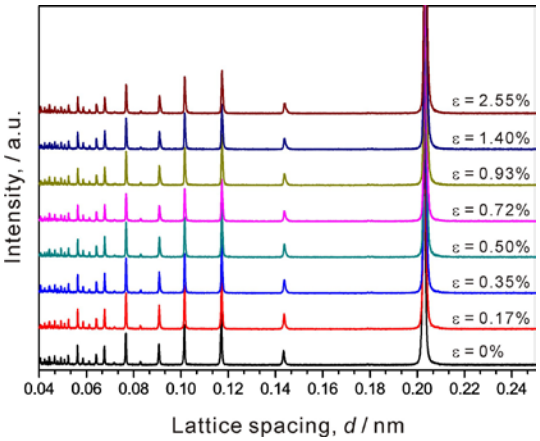

Figure 6 Neutron diffraction profiles of the dual phase steel with various tensile strains.

BL14: 6/23-6/26, 2014

Since the crystal symmetry of the δ_{1p} phase in the Fe-Zn system is hexagonal, there are five independent elastic constants to be uniquely determined. In order to maximize the statistical accuracy of determined elastic constants, it is necessary to measure dispersion of at least five acoustic phonon branches. The acoustic phonon branches were measured around the (3 3 0) and (0 0 28) reflections because they have the largest structural factors. The incident neutron energy was 15 and 13 meV, for the (3 3 0) and (0 0 28) reflections, respectively. The obtained 5D data (Q_x, Q_y, Q_z, energy, intensity) were calibrated along the Q_x, Q_y, Q_z, and energy axes. As can be seen in the Q_x-Q_y slice for the (3 3 0) reflection (Fig. 7(a)), for example, the Q_x and Q_y can be calibrated by shifting them by the amount of ΔQ_x = +0.05 and ΔQ_y = -0.05, respectively. Fig. 7(b) shows an example of obtained phonon dispersions along the Q_y vector ([1-100] direction). From the inclination of the phonon branch near the Γ point as well as the mass density, the corresponding elastic constant, c_{66}, was calculated to be approximately 10.5 GPa. In the same way, other elastic constants c_{11}, c_{33}, and c_{44} were estimated to be 410, 267, and 27 GPa, respectively. The value of c_{12} was deduced to be 389 GPa with the values of c_{11} and c_{66} (c_{66}=(c_{11}-c_{12})/2). The value of c_{13} will be deduced soon by using the phonon dispersion along the (a+c) direction. These values of elastic constants of the δ_{1p} phase

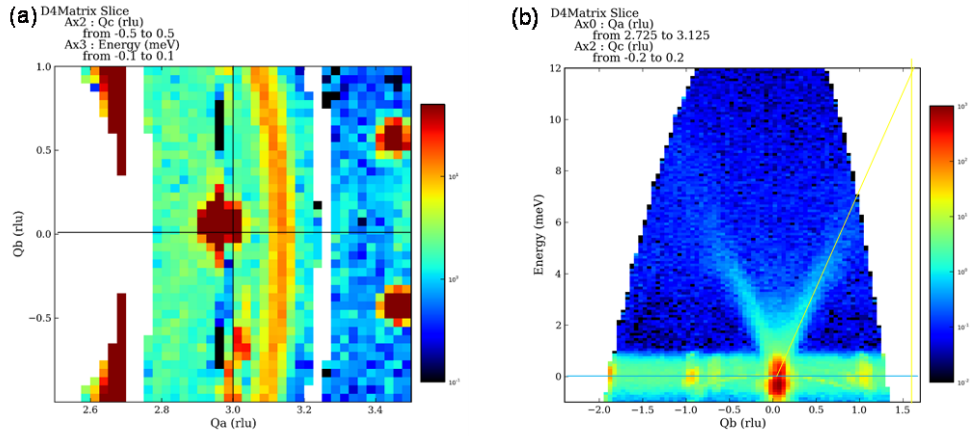

Figure 7 (a) Q_x-Q_y slice for the (3 3 0) reflection. (b) Phonon dispersion along the Q_y vector for the (3 3 0) reflection.